

# Large Rashba spin splitting, double SU(2) spin symmetry, and pure Dirac fermion system in PtSe<sub>2</sub> nanoribbons

Bo-Wen Yu and Bang-Gui Liu\*

*Beijing National Laboratory for Condensed Matter Physics,  
Institute of Physics, Chinese Academy of Sciences, Beijing 100190, China and  
School of Physical Sciences, University of Chinese Academy of Sciences, Beijing 100049, China*

(Dated: December 12, 2023)

Two-dimensional transition metal dichalcogenides host interesting physics and have potential applications in various fields. Recently, it is shown experimentally and theoretically that semiconducting monolayer PtSe<sub>2</sub> nanoflakes with neutral zigzag edges are stable. Here, we study PtSe<sub>2</sub> nanoribbons with the stable edges through first-principles investigation, and find relativistic electron energy dispersion with large Rashba spin splitting in the low-energy bands (even  $N$ ) which originates from the nanoribbon edges. It is shown that there exists SU(2) spin symmetry in both of the conduction and valence bands, which implies conserved spin transport or persistent spin helix (conserved spin structure) along each edge. When the inter-edge interaction becomes weak, a nearly-perfect Dirac fermion system can be achieved for each nanoribbon edge through combining the valence and conduction bands. These electronic systems can realize important effects and could be useful for high-performance spintronic and optoelectronic applications.

## I. INTRODUCTION

Advent of graphene stimulates the huge interest in two-dimensional materials for both basic scientific exploration and practical applications[1–5]. Transition metal dichalcogenides (TMDs) as a typical type of 2D materials have various amazing properties in the field of high-performance electronic, spintronic, and optoelectronic devices[6–8]. Platinum diselenide (PtSe<sub>2</sub>) becomes attractive because PtSe<sub>2</sub> monolayer and multilayers can be made stable on various surfaces[9–12]. Further exploration indicates that the PtSe<sub>2</sub> can host many intriguing properties such as piezoresistivity, spin-layer locking, and semiconductor-metal transition[13–16] and it has potential applications in electronic and optoelectronic devices[12, 17–22]. Furthermore, it is shown experimentally that a new neutral zigzag edge of monolayer PtSe<sub>2</sub> is stable[11]. Considering very interesting properties of other TMD edges[23, 24], it is highly desirable to explore structural and electronic properties of monolayer PtSe<sub>2</sub> with stable zigzag edges[11].

Here, we study the PtSe<sub>2</sub> nanoribbons with the stable neutral zigzag edges through first-principles structural optimization and energy band investigation and further analyses of effective electron models. It is found that the edge-related electronic states are in the semiconductor gap of the monolayer PtSe<sub>2</sub> and the low-energy bands can be fitted well with relativistic dispersion relation. We also find large Rashba spin splitting and exact SU(2) spin symmetry in the low-energy parts of the conduction and valence bands for even  $N$  ( $N$  describes the width of the nanoribbon), which implies that there will be conserved spin transport or persistent spin helices along each edge. Furthermore, nearly-perfect Dirac

fermion systems can be achieved by combining the conduction and valence bands when the inter-edge interaction becomes weak enough.

## II. METHODOLOGY

The first-principles calculations are performed with the projector-augmented wave (PAW) method within the density functional theory[25], implemented in the Vienna Ab-initio simulation package software (VASP) [26]. The generalized gradient approximation (GGA) by Perdew, Burke, and Ernzerhof (PBE) [27] is used as the exchange-correlation functional. The self-consistent calculations are carried out with a  $\Gamma$ -centered ( $12 \times 1 \times 1$ ) Monkhorst-Pack grid for the computational slab model of the nanoribbons[28]. The inter-layer vacuum thickness is set to 25 Å and the inter-edge vacuum separation within the plane is equal to 20 Å. The kinetic energy cutoff of the plane waves is set to 450 eV. The convergence criteria of the total energy and atomic force are set to  $10^{-6}$  eV and 0.01 eV/Å. The spin-orbit coupling (SOC) is taken into account in the band calculation and lattice structure optimization.

## III. RESULT AND DISCUSSION

### A. Monolayer PtSe<sub>2</sub> edges

Usually, a monolayer TMD can assume one of the two stable monolayer structures, H-phase and T-phase. For the layered PtSe<sub>2</sub>, the T-phase is the most stable and the T-phase monolayer is a semiconductor. The T monolayer of PtSe<sub>2</sub> has C<sub>3</sub>-centered symmetry and there are six Se atoms near each Pt atom in the PtSe<sub>2</sub> lattice, as shown in Fig. 1. Similar to graphene monolayer which also has the 120° rotational symmetry, the T monolayer of PtSe<sub>2</sub>

\* bgliu@iphy.ac.cn

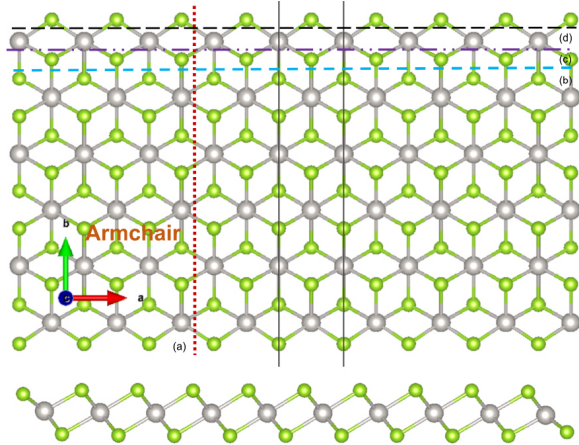


FIG. 1: The structure of the  $\text{PtSe}_2$  nanoribbon with the neutral zigzag edges. The nanoribbon is along the  $a$  axis. The top view shows the  $a$ - $b$  plane (the upper part), and the side view the  $b$ - $c$  plane (the lower part).

can have two types of the edges, armchair edge and zigzag edge. As is shown in Fig. 1, the armchair edge is along the vertical line of  $\text{Pt}-\text{Se}-\text{Se}-\text{Pt}$  and keeps the stoichiometric ratio of  $\text{PtSe}_2$  unchanged, and the zigzag edge is more complex and one can construct three types of edges along the horizontal zigzag direction. Two of the zigzag edges are similar to those of the H phase and have one Pt atom or two Se atoms per unit cell along the edge. There will be net charge on each of these two edges and they tend unstable against reconstruction. The third zigzag edge can be obtained by cutting the lattice through the horizontal dash line and it contains one Se per unit cell along the edge, as shown in Fig. 1. This zigzag edge keeps the correct stoichiometric ratio of  $\text{PtSe}_2$  and charge neutral, and its stability is shown experimentally[11].

In the following, we study the monolayer  $\text{PtSe}_2$  nanoribbon with the stable zigzag edge. This edge can avoid the net charge and keeps the correct edge stoichiometric ratio. Our computational model is shown in Fig. 1. We describe the width of the  $\text{PtSe}_2$  nanoribbon by  $N$  which is the number of the  $\text{PtSe}_2$  units along the perpendicular  $b$  direction. It should be noticed that the symmetry is different between odd  $N$  and even  $N$ . We have optimized the crystal structures with  $N = 3 \sim 10$ . The atomic positions in the interior region are not changed by the optimization, and the atoms near the edges are relaxed with the optimization. The outer-most Se-Pt bond length is shortened by 2.7% (for  $N = 10$ ), and the bond length deviation decreases rapidly when the distance from the edge increases.

## B. Electronic band dispersion

Our test calculation confirms that the monolayer  $\text{PtSe}_2$  is a 2D semiconductor. We study the energy band struc-

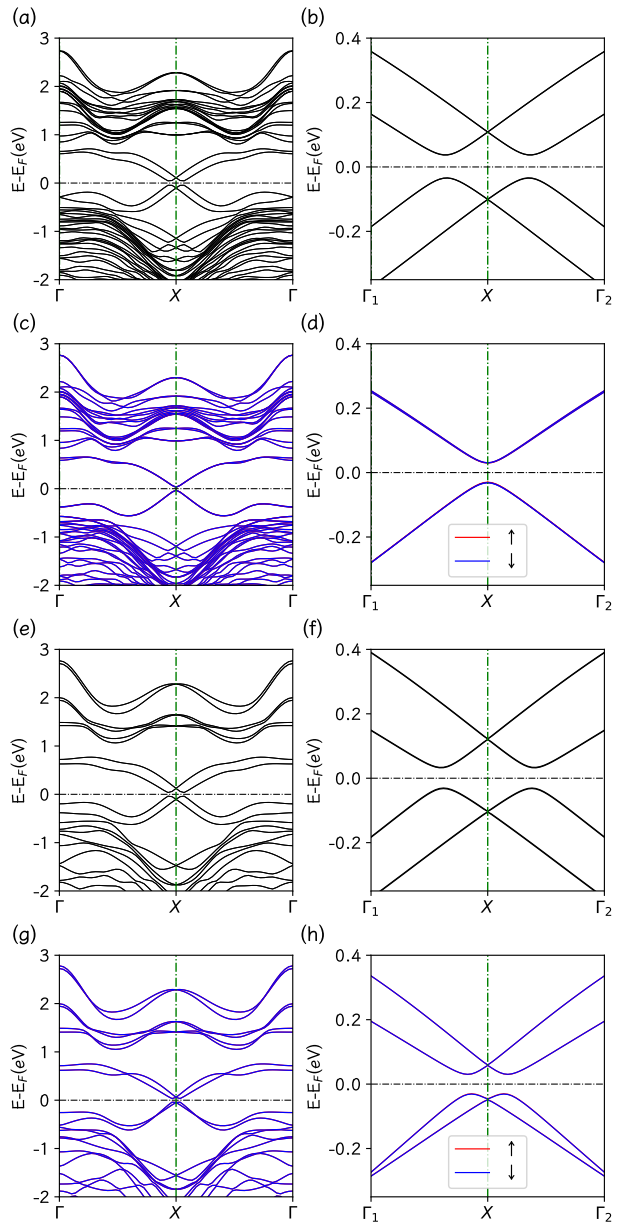


FIG. 2: The band structures of the  $\text{PtSe}_2$  nanoribbons with  $N = 10$  (the upper four panels) and  $N = 4$  (the lower four panels). The left-side panels describe the bands for the entire Brillouin zone, and the right-side panels those near the  $X$  point. The effect of SOC on the bands is demonstrated by showing the bands with (a, b, e, and f) and without (c, d, g, and h) taking SOC into account.

tures of the  $\text{PtSe}_2$  nanoribbons with  $N = 3 \sim 10$ . The electronic structures of the  $\text{PtSe}_2$  nanoribbons with  $N = 10$  and  $N = 4$ , both with and without the SOC taken into account, are presented in Fig. 2. It is clear that there appears some new edge-related bands in the semiconductor gap of the monolayer  $\text{PtSe}_2$ . For the nanoribbon with  $N = 10$ , the band structure without

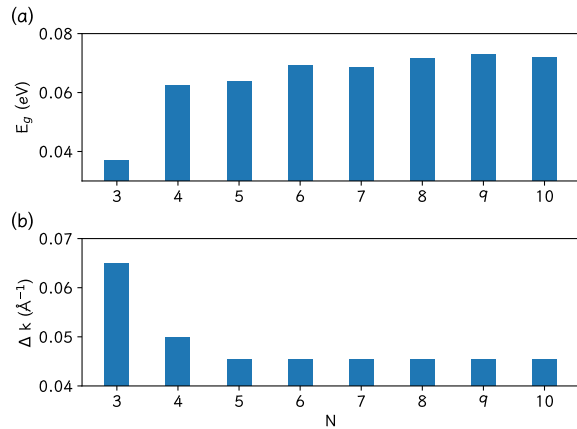


FIG. 3: The  $N$ -dependent energy gaps ( $E_g$  in eV, a) and average  $k$  splitting values ( $\Delta k$ , b) of the  $\text{PtSe}_2$  nanoribbons, with SOC taken into account.  $N$  describes the width of the nanoribbons.

SOC is overall a direct-gap semiconductor and the CBM and VBM are located at the X point in the Brillouin zone. It is very interesting that the conduction bands near the Fermi level can be well fit with a relativistic dispersion relation  $E = \sqrt{\alpha_c p_k^2 + m^2}$  and the corresponding valence bands can be well fit with  $E = -\sqrt{\alpha_v p_k^2 + m^2}$ , where  $p_k$  describes the  $k$  vector with respect to the X point and  $m$  is half of the semiconductor gap. They are both double degenerate for edge and spin.

After taking SOC into account, there appears a large Rashba spin splitting near the X point in the edge-related bands, and both of the VBM and CBM is split into two aside the X point. This double Rashba splitting is different from those in one of the parabolic band edges of conventional semiconductors[29–32]. The two branches of the bands are connected by the relation

$$E_{i\downarrow}(k) = E_{i\uparrow}(k + Q_i), \quad (1)$$

where  $i = c$  ( $i = v$ ) corresponds to the conduction (valence) bands, ( $\uparrow, \downarrow$ ) describes the spin orientation, and  $Q_i$  is the  $k$  difference between the two band extrema. This band symmetry is the same as  $E_{i\uparrow}(k) = E_{i\downarrow}(-k)$ , reflecting the time reversal symmetry. The semiconductor gap is  $E_g = 0.072$  eV and the band dispersion relation read:

$$\begin{aligned} E_{cs} &= \sqrt{\alpha_c^2(p_k - \epsilon_s \gamma_c)^2 + m^2} \\ E_{vs} &= -\sqrt{\alpha_v^2(p_k - \epsilon_s \gamma_v)^2 + m^2}, \end{aligned} \quad (2)$$

where  $s = \uparrow$  or  $\downarrow$ , and  $\epsilon_s = +1$  or  $-1$ , respectively. Here, the parameters are obtained by fitting the calculated bands:  $m = 0.036$  eV,  $\alpha_c = 2.1$  eV $\text{\AA}$ ,  $\alpha_v = 2.2$  eV $\text{\AA}$ ,  $\gamma_c = 0.048$   $\text{\AA}^{-1}$ , and  $\gamma_v = 0.043$   $\text{\AA}^{-1}$ . The parameter  $\gamma_c = Q_c/2$  ( $\gamma_v = Q_v/2$ ) describes the Rashba shift of the CBM (VBM).

For  $N = 4$ , the low-energy bands with SOC can be described well by Eq. (2), too. Here, the parameters are

$m = 0.032$  eV,  $\alpha_c = 2.1$  eV $\text{\AA}$ ,  $\alpha_v = 2.2$  eV $\text{\AA}$ ,  $\gamma_c = 0.054$   $\text{\AA}^{-1}$ , and  $\gamma_v = 0.045$   $\text{\AA}^{-1}$ . It is clear that the low-energy bands with SOC changes little when  $N$  switches from 10 to 4. In contrast, a big change happens in the low-energy bands without SOC. There appear large Rashba-like splitting in the energy bands near both CBM and VBM. This splitting for small  $N = 4$  can be attributed to the interaction between the two edges. It is interesting that this edge-based Rashba-like splitting is similar to the Rashba spin splitting due to SOC.

We present in Fig. 3 the gap  $E_g$  and  $\Delta k = (\gamma_c + \gamma_v)/2$  as the main features of the  $N$  dependent low-energy band structures. A trend can be seen that  $E_g$  increases with  $N$  and  $\Delta k$  decreases with  $N$ . It appears that both  $E_g$  and  $\Delta k$  converge to constants and  $\delta\gamma = |\gamma_c - \gamma_v|$  tends to zero when  $N$  becomes large enough.

### C. Edge feature and Rashba spin splitting

It is interesting to characterize the edge and spin feature in the low-energy bands. First of all, it should be pointed out that in addition to the time reversal symmetry, there exists a space inverse symmetry for odd  $N$ , which makes the energy bands satisfy  $E_{is}(k) = E_{is}(-k)$ . In contrast, the bands for even  $N$  are different, which is necessary to Rashba spin splitting in the bands for even  $N$ . In the following, we shall concentrate our attention on the even  $N$ .

The local density of states (LDOS) is useful to characterize real-space distribution of atomic and orbital weight in the energy bands of the  $\text{PtSe}_2$  nanoribbons. For  $N = 10$ , we have investigated the LDOS of the low-energy bands (in the monolayer gap) of the nanoribbon. It is found that the LDOS is located mainly at the two edges and the LDOS reduces to zero in the middle of the nanoribbon. Therefore, the edge-related bands, especially those low-energy parts, can be attributed to the edges only.

In order to make it clearer, we present in Fig. 4 the key-atom and spin distribution of the low-energy parts of the eight bands near the X point in the Brillouin zone. It is clear that these atomic and spin weights do not change much along the bands near the X point, as shown in Fig. 4. Then, we can characterize the atomic weights by analyzing the atomic weights of the band edges (CBM and VBM). For  $N = 10$ , the Pt and Se atoms in a computational unit cell of the nanoribbon can be numbered as Se1, Pt1, Se2, Se3, Pt2, Se4, …, Se17, Pt9, Se18, Se19, Pt10, Se20. For one Se1+Pt1+Se2+Se3 unit, the summed weight of the conduction band at X is equivalent to 89.2%, and that of the valence band 96.3%. The weight of a Se+Pt+Se unit jumps down and reach zero for the fifth array of Se+Pt+Se unit from the edge. It is also clear in Fig. 4 that the spin x component is zero, the y component is small, and the spin z component is near 1. It can be supposed that the true spin direction can be defined as the y-tilted z direction, and then the true

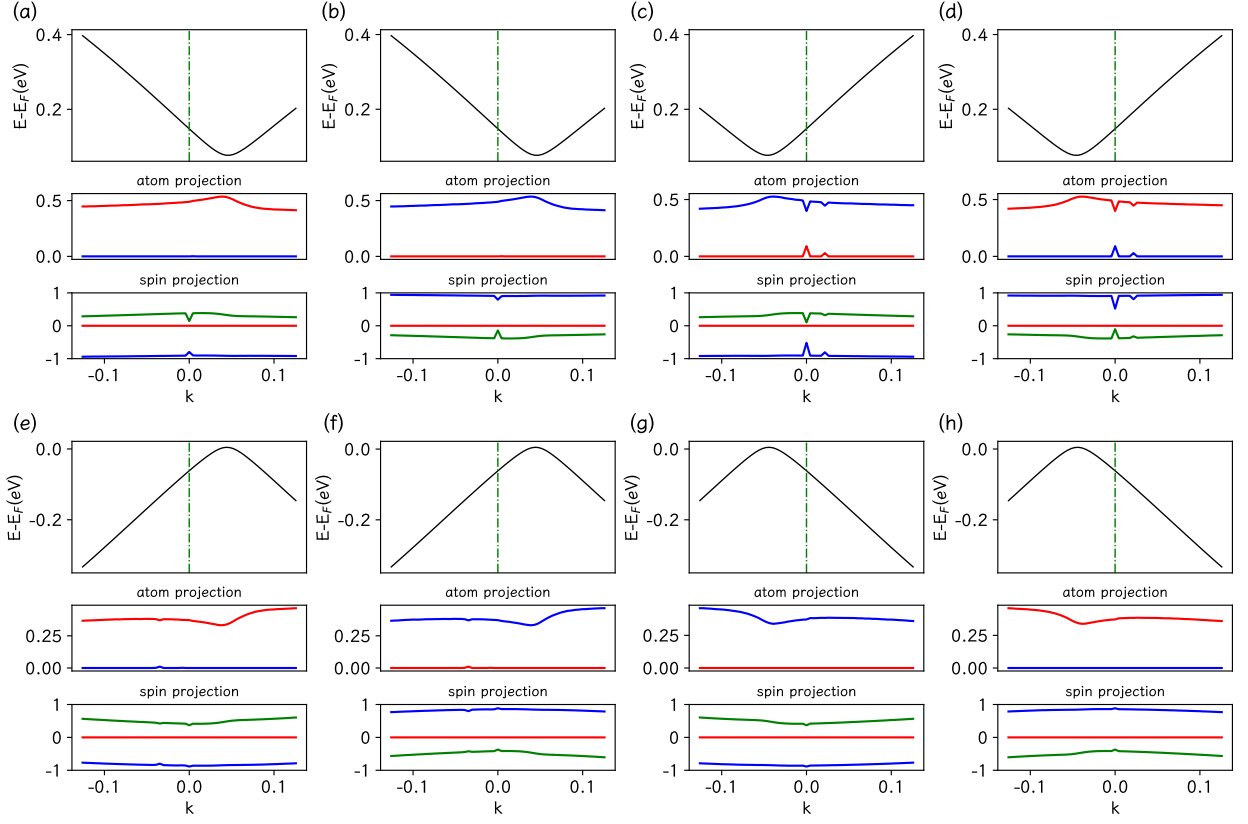


FIG. 4: The edge and spin features of the eight edge-related bands near the X point for  $N = 10$  (a-h). For each of the bands, the atomic projection shows the weight of the Pt atom at the left edge (red line) or that at the right edge (blue line), and the spin projection describes the variation of the three spin components along the band. For the spin projection, the red, green and blue means the  $x$ ,  $y$  and  $z$  directions, respectively. The origin of the coordinate axis is set at the X point in the Brillouin zone.

spin z component is set to 1 and the true y component is also zero. Therefore, it is made clear for even  $N$  that each of the eight low-energy Rashba-split bands are confined to one of the edges and is connected with the true spin components (the z index is still used for the true z component.).

#### D. SU(2) spin symmetry and Dirac fermions

With the characterization of the eight low-energy bands, we can divide the four conduction (valence) bands into two parts so that each of the parts is confined to one of the edges. Thus, we can write the following Hamiltonian for one of the edges.

$$\hat{H} = \sum_{k,s} \left[ \sqrt{\alpha_c^2(k + \epsilon_s \gamma_c)^2 + m^2} c_{kcs}^\dagger c_{kcs} - \sqrt{\alpha_v^2(k + \epsilon_s \gamma_v)^2 + m^2} c_{kvs}^\dagger c_{kvs} \right] \quad (3)$$

where the  $\mathbf{k}$  vector is defined with respect to the X point in the Brillouin zone. For the other edge, the Hamil-

tonian has the same form and the opposite spin due to the time reversal symmetry.

It can be proved that  $[\hat{H}, c_{kis}^\dagger c_{kis}] = 0$  from this Hamiltonian (3). We can construct the following SU(2) spin operators[33],

$$\begin{aligned} S_{iQ_i}^+ &= \sum_k c_{ki\uparrow}^\dagger c_{(k+Q_i)i\downarrow}, \\ S_{iQ_i}^- &= (S_{iQ_i}^+)^{\dagger}, \\ S_i^z &= \frac{1}{2} \sum_k (c_{ki\uparrow}^\dagger c_{ki\uparrow} - c_{ki\downarrow}^\dagger c_{ki\downarrow}), \end{aligned} \quad (4)$$

where  $i = c$  ( $i = v$ ) corresponds to the conduction (valence) bands. It can be proved that these operators obey the following commutation relations.

$$[S_i^z, S_{iQ_i}^\pm] = \pm S_{iQ_i}^\pm, \quad [S_{iQ_i}^+, S_{iQ_i}^-] = 2S_i^z \quad (5)$$

$$[\hat{H}, S_{iQ_i}^\pm] = [\hat{H}, S_i^z] = 0 \quad (6)$$

These results hold independently for CB and VB, and thus there are two series of the SU(2) symmetry

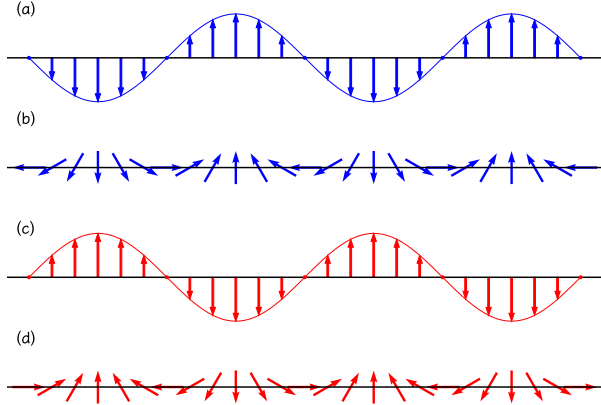


FIG. 5: The persistent spin helices for the conduction bands (a, b) and the valence bands (c, d). The x component is shown in (a) and (c), and the spin vector (in the x-y plane) is described in (b) and (d).

for CB and VB, respectively. These commutation relation show the possibility of persistent spin helix in  $[S^x(Q_c), S^y(Q_c)]$ , which can lead to infinite lifetime of spin polarization[33, 34]. As for the characteristic spatial periodicity of  $l_{\text{PSH}} = \frac{2\pi}{|\mathbf{Q}|}$ , it can be shown that the  $l_{\text{PSH}}$  is equivalent to 6.5 nm (7.1 nm) for the conduction (valence) bands in the case of  $N = 10$ , because of  $Q_c = 0.096 \text{ \AA}^{-1}$  and  $Q_v = 0.088 \text{ \AA}^{-1}$ . In Fig. 5, we show these persistent spin helices of the conduction and valence bands along one of the edges. This short pitch size of PSH can be useful in the future development of high-density scalable spintronic devices[34, 35].

We can show a manifestation of the SU(2) spin symmetry in quantum mechanics. Replacing the hole operator  $h_{kvs}^\dagger$  for the electron  $c_{kvs}$ , we can change Hamiltonian (3) into the following form.

$$\hat{H} = \sum_{k,s} \left[ \sqrt{\alpha_c^2(k + \epsilon_s \gamma_c)^2 + m^2} c_{kcs}^\dagger c_{kcs} + \sqrt{\alpha_v^2(k + \epsilon_s \gamma_v)^2 + m^2} h_{kvs}^\dagger h_{kvs} \right] + E_0 \quad (7)$$

It is clear that the ground state  $|\rangle$  is defined by  $c_{kcs}|\rangle = h_{kvs}|\rangle = 0$ . Suppose we have one doped electron and the lowest states can be described as  $|k, s\rangle = c_{kcs}^\dagger|\rangle$  with  $k = \pm\gamma_c$ . The electron can have the  $\mathbf{k}$  vector  $k = -\gamma_c$  and spin  $s = \uparrow$ , or  $k = \gamma_c$  and  $s = \downarrow$ . For both of the cases,  $|\gamma_c, \uparrow\rangle$  and  $|\gamma_c, \downarrow\rangle$ , the spin z component is conserved and the electron moves with the constant speed.

If the electron takes the following superposition of these two states with a phase difference  $2\lambda_j$ ,

$$|\lambda_j\rangle = e^{-i\lambda_j} |\gamma_c, \uparrow\rangle + e^{i\lambda_j} |\gamma_c, \downarrow\rangle, \quad (8)$$

then the spin z component is not conserved. It can be shown that the state  $|\lambda_j\rangle$  with  $2\lambda_j = 0$  (or  $\pi$ ) is the eigenstate of  $S^x(Q_c)$  with the eigenvalue 1/2 (or -1/2)

(not for  $S^y(Q_c)$ ). We can rotate  $[S^x(Q_c), S^y(Q_c)]$  by  $\theta_j$ , and thus the  $S^x(Q_c)$  is replaced by

$$S^x(Q_c, \theta_j) = S^x(Q_c) \cos(\theta_j) + S^y(Q_c) \sin(\theta_j). \quad (9)$$

Then, we can show that  $|\lambda_j\rangle$  is the eigenstate of  $S^x(Q_c, 2\lambda_j)$  with eigenvalue 1/2. Letting  $\lambda_j = \gamma_c R_j$ , it is clear that the x component  $S^x(Q_c, 2\lambda_j)$  in the rotated frame is conserved in terms of quantum mechanics. If one prepares the initial spin state in a given direction, one will observe a real-space cos pattern (persistent spin density wave) along the direction and the persistent spin helix will be formed in the spin plane including the initial spin direction, as shown in Fig. 5. On the other hand, if we dope a hole in the valence bands, the same result can be obtained. These are consistent with experimental observation in high-mobility electron gases [34, 36, 37] and monolayer WTe<sub>2</sub>[38].

With the  $N$  trend explained above, we believe that when  $N$  is large enough, the symmetry between the conduction bands and the valence bands near the band edges will come true. Then the Hamiltonian (3) can be written as

$$\hat{H} = \sum_{k,j,s} \kappa_j \sqrt{\alpha^2(k + \epsilon_s \gamma)^2 + m^2} c_{kjs}^\dagger c_{kjs}, \quad (10)$$

where  $\kappa_j = 1$  ( $\kappa_j = -1$ ) for  $j = c$  ( $j = v$ ),  $\alpha = \alpha_c = \alpha_v$ , and  $\gamma = \gamma_c = \gamma_v$ . The Hamiltonian (10) can be considered to be the diagonalized version of the following Dirac Hamiltonian.

$$\hat{H} = \sum_{k,s} c_{ks}^\dagger [\alpha(k + \epsilon_s \gamma) \sigma_x + m \sigma_z] c_{ks}, \quad (11)$$

where  $c_{ks}^\dagger = (c_{kcs}^\dagger, c_{kvs}^\dagger)$ , and  $\sigma_x$  and  $\sigma_z$  are the Pauli matrixes describing the conduction and valence bands near the band edges ( $c, v$ ). This Hamiltonian (11) can describe the charge and spin of the nearly-perfect pure Dirac fermion system in one dimension.

#### IV. CONCLUSION

We have investigated the PtSe<sub>2</sub> nanoribbons with the stable neutral zigzag edges through first-principles structural optimization and electronic structure calculation and further analyses of their energy bands. We find that the edge-related energy bands are in the semiconductor gap of the monolayer PtSe<sub>2</sub> and the low-energy part of them can be fitted well with relativistic electron energy dispersions with large Rashba spin splitting for even  $N$ . Our analysis of atom-projected band structures and densities of states indicates that each of the low-energy bands originate from one of the nanoribbon edges. More importantly, it is shown that there exists SU(2) spin symmetry in both of the conduction and valence low-energy bands, which implies conserved spin transport or persistent spin helix along each edge. Furthermore, when

the inter-edge interaction becomes weak, a nearly-perfect Dirac fermion system can be achieved for each nanoribbon edge through combining the valence and conduction bands. These electronic systems realize these important effects and could be useful for future high-performance applications[4, 5, 39].

## ACKNOWLEDGMENTS

This work is supported by the Strategic Priority Research Program of the Chinese Academy of Sciences (Grant No. XDB33020100) and the Nature Science Foundation of China (Grant No.11974393) . All the numerical calculations were performed in the Milky Way #2 Supercomputer system at the National Supercomputer Center of Guangzhou, Guangzhou, China.

---

[1] K. S. Novoselov, A. K. Geim, S. V. Morozov, D.-E. Jiang, Y. Zhang, S. V. Dubonos, I. V. Grigorieva, and A. A. Firsov, *Science* **306**, 666 (2004).

[2] A. C. Neto, F. Guinea, N. M. Peres, K. S. Novoselov, and A. K. Geim, *Reviews of Modern Physics* **81**, 109 (2009).

[3] A. K. Geim, *Science* **324**, 1530 (2009).

[4] Y. Liu, X. Duan, H.-J. Shin, S. Park, Y. Huang, and X. Duan, *Nature* **591**, 43 (2021).

[5] J. Jiang, L. Xu, C. Qiu, and L.-M. Peng, *Nature* **616**, 470 (2023).

[6] M. Chhowalla, H. S. Shin, G. Eda, L.-J. Li, K. P. Loh, and H. Zhang, *Nature Chemistry* **5**, 263 (2013).

[7] M. Chhowalla, D. Jena, and H. Zhang, *Nature Reviews Materials* **1**, 1 (2016).

[8] Y. Wang, J. Z. Ou, S. Balendhran, A. F. Chrimes, M. Mortazavi, D. D. Yao, M. R. Field, K. Latham, V. Bansal, J. R. Friend, *et al.*, *ACS Nano* **7**, 10083 (2013).

[9] F. A. Rasmussen and K. S. Thygesen, *The Journal of Physical Chemistry C* **119**, 13169 (2015).

[10] M. O'Brien, N. McEvoy, C. Motta, J.-Y. Zheng, N. C. Berner, J. Kotakoski, K. Elibol, T. J. Pennycook, J. C. Meyer, C. Yim, M. Abid, T. Hallam, J. F. Donegan, S. Sanvito, and G. S. Duesberg, *2D Materials* **3**, 021004 (2016).

[11] J. Li, T. Joseph, M. Ghorbani-Asl, S. Kolekar, A. V. Krasheninnikov, and M. Batzill, *Advanced Functional Materials* **32**, 2110428 (2022).

[12] Y. Wang, L. Li, W. Yao, S. Song, J. Sun, J. Pan, X. Ren, C. Li, E. Okunishi, Y.-Q. Wang, *et al.*, *Nano Letters* **15**, 4013 (2015).

[13] W. Yao, E. Wang, H. Huang, K. Deng, M. Yan, K. Zhang, K. Miyamoto, T. Okuda, L. Li, Y. Wang, *et al.*, *Nature Communications* **8**, 14216 (2017).

[14] S. Wagner, C. Yim, N. McEvoy, S. Kataria, V. Yokaribas, A. Kuc, S. Pindl, C.-P. Fritzen, T. Heine, G. S. Duesberg, and M. C. Lemme, *Nano Letters* **18**, 3738 (2018).

[15] X. Lin, J. C. Lu, Y. Shao, Y. Y. Zhang, X. Wu, J. B. Pan, L. Gao, S. Y. Zhu, K. Qian, Y. F. Zhang, D. L. Bao, L. F. Li, Y. Q. Wang, Z. L. Liu, J. T. Sun, T. Lei, C. Liu, J. O. Wang, K. Ibrahim, D. N. Leonard, W. Zhou, H. M. Guo, Y. L. Wang, S. X. Du, S. T. Pantelides, and H. J. Gao, *Nature Materials* **16**, 717 (2017).

[16] Y. Zhao, J. Qiao, Z. Yu, P. Yu, K. Xu, S. P. Lau, W. Zhou, Z. Liu, X. Wang, W. Ji, *et al.*, *Advanced Materials* **29**, 1604230 (2017).

[17] Z. Wang, Q. Li, F. Besenbacher, and M. Dong, *Advanced Materials* **28**, 10224 (2016).

[18] C. Yim, K. Lee, N. McEvoy, M. O'Brien, S. Riazimehr, N. C. Berner, C. P. Cullen, J. Kotakoski, J. C. Meyer, M. C. Lemme, *et al.*, *ACS Nano* **10**, 9550 (2016).

[19] C. Yim, N. McEvoy, S. Riazimehr, D. S. Schneider, F. Gity, S. Monaghan, P. K. Hurley, M. C. Lemme, and G. S. Duesberg, *Nano Letters* **18**, 1794 (2018).

[20] L.-H. Zeng, S.-H. Lin, Z.-J. Li, Z.-X. Zhang, T.-F. Zhang, C. Xie, C.-H. Mak, Y. Chai, S. P. Lau, L.-B. Luo, *et al.*, *Advanced Functional Materials* **28**, 1705970 (2018).

[21] J. Yuan, H. Mu, L. Li, Y. Chen, W. Yu, K. Zhang, B. Sun, S. Lin, S. Li, and Q. Bao, *ACS Applied Materials & Interfaces* **10**, 21534 (2018).

[22] L. Tao, X. Huang, J. He, Y. Lou, L. Zeng, Y. Li, H. Long, J. Li, L. Zhang, and Y. H. Tsang, *Photonics Research* **6**, 750 (2018).

[23] P. Chen, W. W. Pai, Y.-H. Chan, W.-L. Sun, C.-Z. Xu, D.-S. Lin, M. Chou, A.-V. Fedorov, and T.-C. Chiang, *Nature Communications* **9**, 2003 (2018).

[24] S. Tang, C. Zhang, D. Wong, Z. Pedramrazi, H.-Z. Tsai, C. Jia, B. Moritz, M. Claassen, H. Ryu, S. Kahn, *et al.*, *Nature Physics* **13**, 683 (2017).

[25] P. E. Blöchl, *Phys. Rev. B* **50**, 17953 (1994).

[26] G. Kresse and J. Hafner, *Phys. Rev. B* **47**, 558 (1993).

[27] J. P. Perdew, K. Burke, and M. Ernzerhof, *Physical Review Letters* **77**, 3865 (1996).

[28] H. J. Monkhorst and J. D. Pack, *Phys. Rev. B* **13**, 5188 (1976).

[29] E. Rashba, *Sov. Phys. Solid State* **2**, 1109 (1960).

[30] E. Rashba, *Journal of Electron Spectroscopy and Related Phenomena* **201**, 4 (2015).

[31] A. Manchon, H. C. Koo, J. Nitta, S. M. Frolov, and R. A. Duine, *Nature Materials* **14**, 871 (2015).

[32] G. Bihlmayer, P. Noel, D. V. Vyalikh, E. V. Chulkov, and A. Manchon, *Nature Reviews Physics* **4**, 642 (2022).

[33] B. A. Bernevig, J. Orenstein, and S.-C. Zhang, *Physical Review Letters* **97**, 236601 (2006).

[34] J. Schliemann, *Reviews of Modern Physics* **89**, 011001 (2017).

[35] A. Avsar, H. Ochoa, F. Guinea, B. Ozyilmaz, B. J. van Wees, and I. J. Vera-Marun, *Reviews of Modern Physics* **92**, 021003 (2020).

[36] J. D. Koralek, C. P. Weber, J. Orenstein, B. A. Bernevig, S.-C. Zhang, S. Mack, and D. D. Awschalom, *Nature* **458**, 610 (2009).

[37] M. P. Walser, C. Reichl, W. Wegscheider, and G. Salis, *Nature Physics* **8**, 757 (2012).

[38] J. H. Garcia, M. Vila, C.-H. Hsu, X. Wainta, V. M. Pereira, and S. Roche, *Physical Review Letters* **125**, 256603 (2020).

[39] W. Cao, H. Bu, M. Vinet, M. Cao, S. Takagi, S. Hwang, T. Ghani, and K. Banerjee, *Nature* **620**, 501 (2023).